Journal of Materials Chemistry A

ROYAL SOCIETY OF CHEMISTRY

PAPER

View Article Online
View Journal

Open Access Article. Published on 23 January 2026. Downloaded on 2/25/2026 12:13:14 PM.
This article is licensed under a Creative Commons Attribution-NonCommercial 3.0 Unported Licence.

Check for updates

Cite this: DOI: 10.1039/d5ta09855f

A spontaneous water-detaching hydrophobic coating resistant to calendar aging based on non-equilibrium wetting

Jiaxue Yu, Wenting Wang, Yifan Li, Zilin Ye, Qiuhong Zhang * and Xudong Jia*

Received 2nd December 2025
Accepted 22nd January 2026

DOI: 10.1039/d5ta09855f

rsc.li/materials-a

Hydrophobic surfaces can spontaneously remove adhering water and dust due to their unique "lotus effect", offering significant value in self-cleaning, anti-icing, drag reduction, and anti-contamination fields. However, compared to natural hydrophobic surfaces, artificially engineered counterparts often suffer from inherent limitations, among which the rapid degradation of hydrophobicity remains one of the most critical barriers to their widespread application. Moreover, the underlying mechanism governing this decay process is still not sufficiently clear. To address these challenges, we propose to divide wetting behavior into two categories: equilibrium wetting and non-equilibrium wetting. The proposal suggests that the accumulation of contaminants under non-equilibrium wetting conditions plays a pivotal role in the deterioration of surface hydrophobicity. Based on this insight, we develop a water-based coating which can generate a spontaneous water-detaching surface that is resistant to calendar aging and can maintain a durable hydrophobic effect under diverse outdoor climate conditions.

Introduction

Heavy rainfall has become a matter of concern in recent years,[1,2] and studies have demonstrated that anthropogenic influences have significantly altered the precipitation patterns associated with tropical cyclones in the Western North Pacific (WNP) region.[3,4] Since 1961, the frequency of extreme rainfall events has markedly increased along the East Asian coast,[5] and since 2000, this scene has become widespread globally.[6] The increase in precipitation has also brought significant challenges, including acid rain leading to deterioration of building materials,[7,8] severe threat to the power grid from freezing rain,[9] and increasing pressure on indoor and outdoor humidity management due to frequent humidity fluctuations.[10,11] These phenomena influence our lives through a series of wetting and dewetting behaviors. Hydrophobic surfaces, which promote the spontaneous removal of water from surfaces, offer a promising solution to these challenges. Over the past few decades, substantial research efforts have been devoted to the development of high-performance hydrophobic surfaces.

Hydrophobic surfaces have attracted wide attention due to their ability to induce water shedding, and foundational work has been conducted in interfacial wetting models. Young's equation first described wettability based on the contact angle formed by equilibrium interfacial tensions.[12] Wenzel[13] and Cassie–Baxter[14] subsequently refined these models to better represent the solid–liquid interface, making major contributions to the theoretical understanding of wetting behavior. Contact angle serves as a key metric in evaluating surface hydrophobicity in these theories, which are based on force equilibrium at the solid-liquid-gas three-phase contact line, in the framework of Newtonian mechanics. However, due to the inherently dynamic and deformable nature of water under real-world conditions, these conventional models are usually inadequate for explaining transient wetting phenomena, such as the impact of water droplets on solid surfaces, as it is challenging to identify a state where the interfacial forces balance to zero.[15,16] As a result, developing theoretical frameworks capable of understanding wetting behaviors under non-equilibrium force conditions remains a significant challenge.

Another latent challenge is the unclear mechanism of hydrophobicity degradation, which, in common sense, is primarily attributed to the fragility of surface textures. Recent advances have improved the durability of hydrophobic surfaces by surface chemical modification,[17–19] precise micro-nano texturing,[20–25] self-healing mechanisms,[26–28] phase separation,[29] and bio-based biomimetic strategies.[30–32] These methods have extended the functional lifetimes of hydrophobic coatings to some extent. However, the mechanism by which environmental exposure alters surface structure is still poorly understood, and achieving long-term hydrophobic stability under natural conditions remains a formidable challenge.

In this study, we propose a new approach to describe hydrophobic performance. Inspired by the relationship between Newtonian mechanics and Lagrangian mechanics, we extend the classical wetting models. Wetting behaviors are

Department of Polymer Science and Engineering, School of Chemistry and Chemical Engineering, Nanjing University, Nanjing 210023, P. R. China. E-mail: chemzqh@nju.edu,cn; jiaxd@nju.edu.cn

Open Access Article. Published on 23 January 2026. Downloaded on 2/25/2026 12:13:14 PM.
This article is licensed under a Creative Commons Attribution-NonCommercial 3.0 Unported Licence.

classified into equilibrium state and non-equilibrium state. The new interface generated by non-equilibrium wetting leads to the accumulation of impurities on the surface. This behavior, occurring continuously in nature, is a key factor contributing to hydrophobic degradation.[33,34] Based on these insights, we developed a water-based hydrophobic coating, denoted as SP@HNP, which maintained long-lasting hydrophobicity across various climate conditions. The on-site deployment in multiple cities with diverse climates confirmed that the coating sustained its hydrophobicity for more than nine months in all tested regions. To evaluate scalability, we successfully synthesized one ton of hydrophobic coating and sprayed it onto the surface of the umbrella. The resulting hydrophobic umbrellas effectively prevented water adhesion, thereby mitigating the substantial carbon emissions and microplastic generation typically associated with wet umbrella management. This work thus offers a sustainable and scalable solution for preparing hydrophobic coatings, reducing environmental burden arising from intensified precipitation due to climate change.

Results and discussion

Wetting behavior of hydrophobic surfaces

Hydrophobic surfaces have garnered sustained interest over the past two centuries due to their broad technological relevance. A rigorous and physically grounded metric is essential for accurately quantifying surface hydrophobicity. Extensive efforts have been dedicated to the development of wetting models. Young's classical model describes that the solid–liquid interface replaces the solid–gas interface and is driven by interfacial tension at the phase boundary (Fig. S1). At equilibrium, the interfacial tensions at the three-phase contact line must sum to zero, and the liquid phase should be either stationary or moving at a constant velocity.[12] However, achieving perfect equilibrium in the real world remains challenging. As a result, there are still discrepancies when using Young's equation to describe actual wetting behavior. Subsequent refinements to Young's model incorporate the concepts of surface roughness (Fig. S2) and multi-phase coexistence (Fig. S3), as proposed by Wenzel[13] and Cassie,[14] respectively.

Despite these theoretical advancements, classical wetting models often fall short in capturing the complexity of real-world wetting phenomena. For example, McCarthy *et al.* demonstrated that contact angle hysteresis was as critical as the contact angle itself in characterizing wetting behavior[35] (Fig. S4); Lafuma *et al.* observed a significant change in contact angle upon the variation of liquid volume[33] (Fig. S5); Jiang *et al.* reported that even when inverted by 180°, liquids might remain firmly adhered to the superhydrophobic surface due to interface adhesion force[36–40] (Fig. S6). These inconsistencies underscore the intrinsic limitation of using a single contact angle to describe wetting behavior, as it is inherently volume dependent. In most wetting systems, the liquid properties remain unchanged, while the surface properties of the solid are the primary variable of interest. Classical models, based on roughness (Wenzel) or multi-phase coexistence (Cassie), implicitly assume that droplet size greatly exceeds surface feature dimensions. However, this size mismatch is at the origin of contact angle hysteresis. As such, incorporating contact angle hysteresis is essential for accurately characterizing hydrophobic surfaces under practical conditions.

Despite these insights, the variability in droplet size continues to pose significant challenges to the quantitative characterization of solid surface wettability. To address this limitation, we propose a novel framework inspired by Lagrangian mechanics and Hamilton's principle by analyzing wetting transitions between the initial and final states. We classify wetting behavior into equilibrium and non-equilibrium regimes (Fig. 1). Equilibrium wetting behavior can be described by the apparent contact angle of a liquid with a specific volume (Newtonian mechanics), while non-equilibrium wetting behavior can be characterized by the types and magnitudes of energy within the system (Lagrangian mechanics). In equilibrium wetting, macroscopic forces remain unchanged, and Newtonian mechanics facilitates the application of interfacial

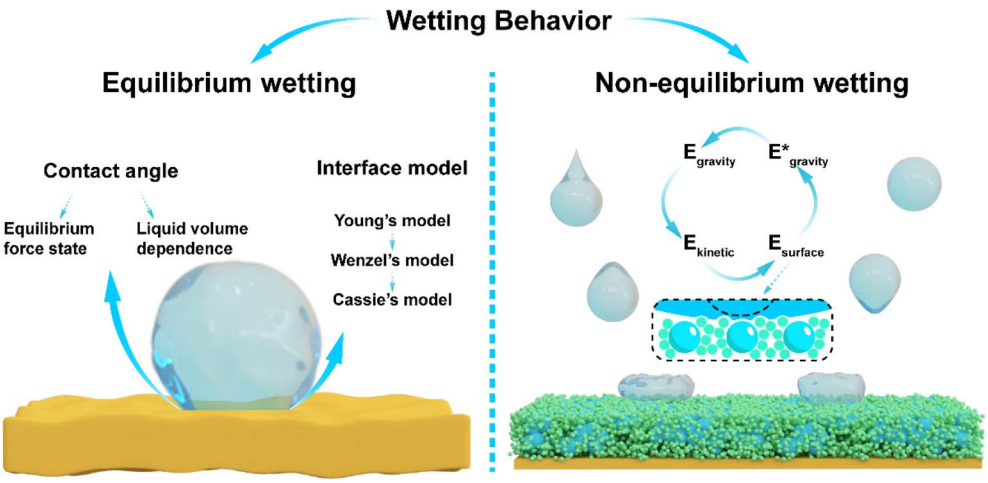

Fig. 1 Wetting behaviors categorized into equilibrium wetting and non-equilibrium wetting.

Open Access Article. Published on 23 January 2026. Downloaded on 2/25/2026 12:13:14 PM.
This article is licensed under a Creative Commons Attribution-NonCommercial 3.0 Unported Licence.

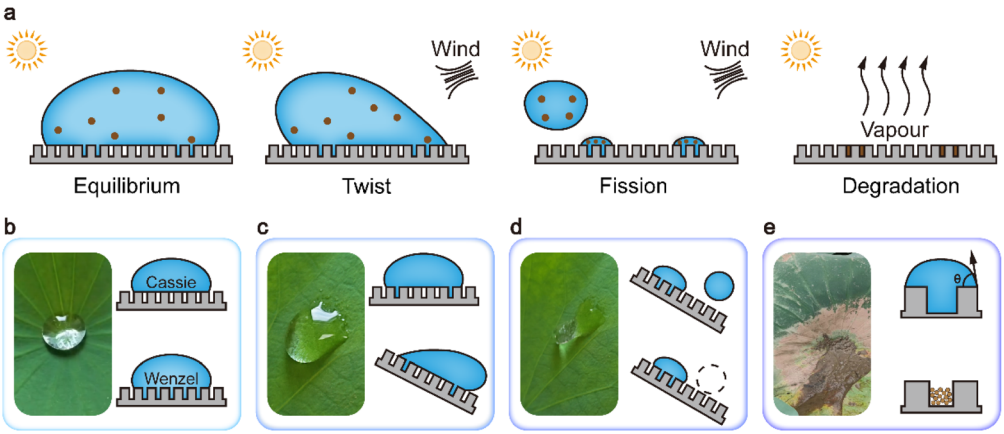

Fig. 2 Mechanism of surface hydrophobicity degradation induced by non-equilibrium wetting. (a) Schematic illustration of surface hydrophobicity degradation induced by non-equilibrium wetting. (b) Wetting model of water droplets on a lotus leaf surface, existing in a mixed state of Wenzel and Cassie models. (c) The droplet seeks a new equilibrium state by increasing its surface area. (d) The droplet seeks a new equilibrium state through fission. (e) Progressive accumulation of contaminants triggers irreversible structural transformations at the surface, resulting in diminished hydrophobicity.

tension. The angle of interfacial tensions is a function that depends solely on the liquid volume and surface hydrophobicity (the liquid properties remain unchanged), enabling the assessment of solid surface hydrophobicity by fixing the liquid volume. In non-equilibrium wetting, the force, velocity, shape, and volume of the liquid are time-dependent variables. Drawing inspiration from the concepts of "degrees of freedom" in Lagrangian mechanics and the principle of path integration in Hamilton's principle, non-equilibrium wetting on hydrophobic surfaces can be articulated as follows: the total energy of the solid–liquid system at the initial (E_0) and final (E_0') states is conserved, encompassing energy transformations involving kinetic energy (E_k), gravitational potential energy (E_g), surface energy (E_s), and interfacial energy (E_i). Each energy state can be expressed as a time-dependent function. Due to the variability in liquid size during non-equilibrium wetting, it is difficult to directly measure this function. However, by analyzing the types and magnitudes of energy transformations, the hydrophobicity of the surface can be further classified.

During the non-equilibrium wetting process on hydrophobic surfaces, water droplets undergo a series of distinct energy transitions that reflect the wetting characteristics of the surface. The evaluation of hydrophobicity in this regime hinges on understanding these energy transformations. As a stationary droplet accelerates under gravity, its gravitational potential energy is progressively converted into kinetic energy. Upon impacting with the solid surface, this kinetic energy peaks. However, due to the resistance from the hydrophobic substrate, the kinetic energy of droplet rapidly dissipates. To compensate, the droplet increases its surface area, resulting in an increase in surface energy (surface area expanding by overcoming surface tension). This transition is accompanied by a notable morphological change—from a compact "coconut" shape to a more flattened "pizza" configuration. Throughout this deformation process, a portion of the kinetic energy is also redistributed into interfacial energy (wetting work of molecular interactions at the solid–liquid interface). The competition and conversion between surface energy and interfacial energy are fundamentally modulated by the degree of surface hydrophobicity, thus offering an indirect yet insightful metric for assessing wetting behavior under dynamic conditions. The generation of interfacial energy signifies the formation of a new solid–liquid interface, which requires additional work to overcome adhesion and detach the droplet from the surface (Fig. S7). In contrast, when the kinetic energy of a droplet is fully converted into surface energy without the generation of interfacial energy, the droplets can spontaneously leave the surface and be driven solely by surface energy (or residual kinetic energy) without additional energy input.

Mechanism of hydrophobicity degradation under non-equilibrium wetting

The rapid degradation of hydrophobicity remains a major obstacle for the practical and large-scale deployment of hydrophobic surfaces. A comprehensive understanding of the non-equilibrium wetting process is essential for the rational design of chemical compositions and surface morphologies, ultimately enabling the development of durable and long-lasting hydrophobic interfaces. While conventional studies have emphasized the role of micro-nano structured surfaces in sustaining hydrophobicity, such delicate architectures are inherently susceptible to mechanical damage during use, often resulting in irreversible performance loss. Therefore, a central strategy for engineering hydrophobic surfaces lies in designing robust architectures capable of preserving their structural integrity under operational conditions. In this study, we advance the understanding of hydrophobic degradation by introducing the concept of non-equilibrium wetting. We propose that the dynamic formation of new solid–liquid interfaces under non-equilibrium conditions plays a pivotal role in perturbing surface micro-nanostructures, thereby accelerating the loss of hydrophobicity. Under natural conditions, air

Open Access Article. Published on 23 January 2026. Downloaded on 2/25/2026 12:13:14 PM.
This article is licensed under a Creative Commons Attribution-NonCommercial 3.0 Unported Licence.

contains a large amount of dust and microplastics, which interact with hydrophobic surfaces through precipitation or condensation, a process inherent to the natural water cycle.[34,41–44] Once solid–liquid interfaces are formed during non-equilibrium wetting, dust and microplastics will remain attached to the surface. Although water can be returned to the natural environment through evaporation, those contaminants still adhere to the surface. Residual contaminants on the surface can diminish hydrophobicity by gradually filling fragile textures or altering the chemical composition of the surface. Therefore, hydrophobic surfaces resistant to calendar aging must be able to withstand the challenges posed by contaminant accumulation induced by the water cycle throughout the aging process (Fig. 2a).

This mechanism of hydrophobicity degradation provides a theoretical basis for understanding the natural formation of a spontaneous water-detaching surface (SWDS). A quintessential example is the lotus leaf, which has attracted considerable attention for its extraordinary ability to remain "unstained by the mud". After rainfall, water tends to accumulate in the micro-depressions on the leaf surface, where high-velocity droplets initially undergo non-equilibrium wetting. Under equilibrium conditions, the wetting state represents a hybrid of the Cassie and Wenzel models (Fig. 2b). External factors, such as wind, can disrupt the wetting state and drive the system toward a new equilibrium. However, due to the irreversibility of the wetting process, this transition is not reversible. Initially, water increases its surface area by distorting its shape, which is manifested as contact angle hysteresis (Fig. 2c). As the shape deformation becomes insufficient to restore equilibrium, the water droplet undergoes fragmentation in pursuit of a new balance. The high-energy portions of the droplet detach from the surface, while the remaining part establishes a new equilibrium with the substrate (Fig. 2d). This process also provides a pathway for the accumulation of contaminants at the interface. Under certain climatic conditions, long-term accumulation can induce irreversible changes in the surface structure, ultimately leading to degradation of hydrophobicity (Fig. 2e). Nonetheless, owing to its biological vitality, the surface structure of the lotus leaf undergoes continuous regeneration. This self-renewal mechanism to resist the accumulation of stains is a unique characteristic of living organisms. However, the fabrication of biomimetic structures *via* chemical routes remains a huge challenge.

Spontaneous water detachment enabled by robust multi-scale architecture

To prevent the impact of new interfaces on hydrophobicity during non-equilibrium wetting, we developed a water-based hydrophobic coating (SP@HNP) with micro to mesoscale roughness and low surface energy, effectively suppressing the conversion of kinetic energy into interfacial energy during non-equilibrium wetting. This resulted in a SWDS that maintained its performance over extended calendar aging. SP@HNP was composed of a dispersion of hydrophobic nanoparticles (HNPs) in ethanol and a waterborne polyurethane emulsion (SP). The HNPs were synthesized *via* a sol–gel process, in which the tetraethyl orthosilicate (TEOS) precursor underwent hydrolysis under the catalysis of ammonium hydroxide to form silica nanoparticles, followed by further heptadecafluorodecyltrimethoxysilane (FAS-17) modification of the nascent particles (Fig. S8A). SEM analysis revealed that the size of the nascent particles was relatively uniform, with an average diameter of approximately 120 nm (Fig. S8B). After further hydrolysis, the particle size increased, and partial cross-linking between particles occurred (Fig. S8C). The resulting particles were dispersed in ethanol and subjected to high-speed shear mechanical forces, leading to the formation of a narrow particle size distribution in the HNP ethanol dispersion (Fig. S9). As a water-based adhesive, SP emulsion must exhibit affinity for both the HNPs and the substrate, and also contribute to the low surface energy and structural robustness of the final coating. Si–O–C bonds are incorporated in polyurethane to enhance the affinity between polyurethane and HNPs (Fig. S10 and 11). By preparing an anionic emulsion, the Si–O–C bonds are effectively concealed in the oil-phase core, preventing them from reacting with water, and ensuring that the Si–O–C bonds together with the HNPs can form a low-surface-energy and robust structure during the curing process of the coating. We adjusted the raw material ratios to prepare a series of SP emulsions (Fig. S12 and Table S1). FT-IR analysis shows that the relative intensities of the ester carbonyl stretching at 1705 cm^{-1} and the amide carbonyl stretching at 1645 cm^{-1} are consistent with the structural design proportions (Fig. S13). Powder XRD data shows that the SP films exhibit broad peaks at $2\theta = 19°$, corresponding to the amorphous structure of polyurethane (Fig. S14). As the content of Si–O–C bonds increases, the intensity of the amorphous peak decreases, indicating that the introduction of Si–O–C bonds affects the original ordered structure of polyurethane, leading to a gradual reduction of the order degree. DLS measurements indicate that the SP emulsions (except for SP-4) exhibit a narrow particle size distribution, and as the Si–O–C bond content on the PU chain increases, the emulsion particle size also increases (Fig. S15). We hypothesize that the presence of Si–O–C bonds increases the crosslinking probability between chains, thereby resulting in a larger oil-phase size.

The SP emulsion was mixed with the HNP ethanol dispersion and sprayed onto the substrate surface. After water and ethanol fully evaporated at room temperature, a hydrophobic surface was obtained. The non-equilibrium wetting behavior of low-velocity water droplets on SP-(0-5)@HNP was observed by a high-speed camera (Fig. 3a, Movie S1-5). Notably, SP-5 exhibited an optimal ratio of functional groups, enabling it to effectively balance the internal cohesion and interfacial adhesion of the coating. Thus, only SP-5@HNP can effectively prevent energy conversion into interfacial energy during the non-equilibrium wetting process (Fig. 3a, Movie S6). SEM analysis revealed that the SP-5@HNP surface had a hierarchical structure with a roughened texture. However, a roughened texture alone was not sufficient for SWDS formation. For SP-1@HNP, SP-2@HNP, SP-3@HNP, and SP-4@HNP that did not exhibit an SWDS, distinct flat regions were observed in the

 This journal is © The Royal Society of Chemistry 2026

Open Access Article. Published on 23 January 2026. Downloaded on 2/25/2026 12:13:14 PM.
This article is licensed under a Creative Commons Attribution-NonCommercial 3.0 Unported Licence.

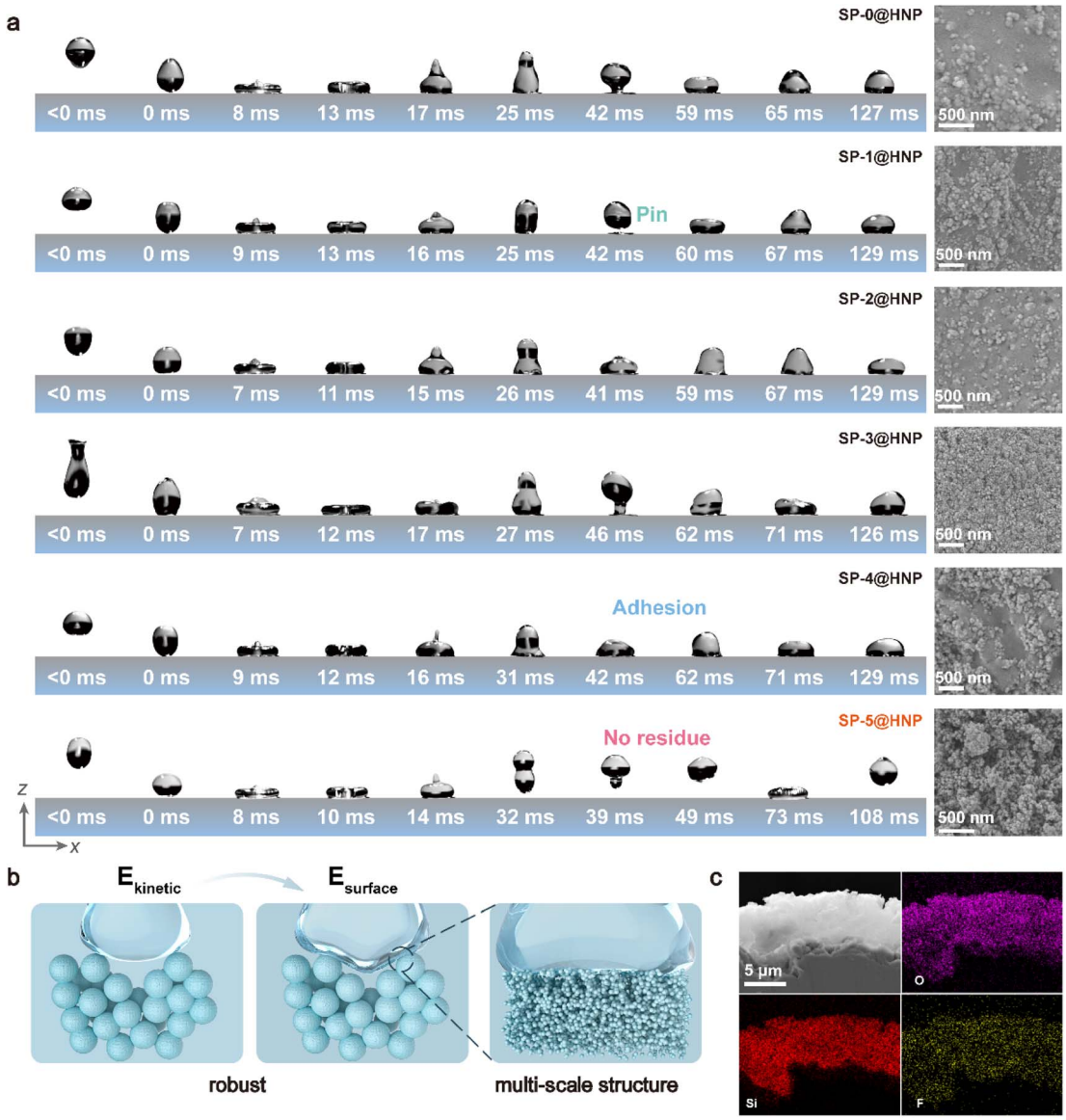

Fig. 3 Surface structures of SP-(0-5)@HNP and the non-equilibrium wetting behavior of low-velocity ($v \approx 0.64$ m s^{-1}) water droplets on their surfaces. (a) High-speed camera images depicting the non-equilibrium wetting of low-velocity water droplets on the surfaces of SP-(0-5)@HNP and SEM images of their surface structures. (b) Schematic representation of the structure of the SWDS. (c) Energy dispersive spectroscopy (EDS) characterization of SP-5@HNP.

microstructures (Fig. 3a). These regions failed to entrap air and sustain the Cassie state as the solid–liquid contact area expanded during non-equilibrium wetting, resulting in interfacial energy accumulation. The generated interfacial energy prevented the liquid from detaching from the surface within its own intrinsic energy. In contrast, the SWDS not only possessed rough structures with a high specific surface area but also featured finer-scale roughness to accommodate variations in liquid volume (Fig. 3b). EDS analysis confirmed that the SWDS exhibited a uniform elemental distribution along with a broad range of roughness features (Fig. 3c). Based on these findings, we identified two critical demands for SWDS formation. (i) Constructing a robust surface structure to ensure structural stability during non-equilibrium wetting. A substantial incorporation of Si–O–C linkages facilitates amphiphilic adhesion by bridging hydrophilic and hydrophobic interfaces. Concurrently, the formation of crosslinked Si–O–Si networks provides significant mechanical stability, contributing to improved system robustness. (ii) Forming a multi-scale structural framework to buffer the variations in liquid volume occurring during the wetting process.

Mechanism of SWDS formation *via* solvent evaporation

Since the SP-5@HNP composite exhibited excellent spontaneous water repellency under non-equilibrium wetting conditions, we thus hypothesized that the incorporation of Si–O–C bonds could strengthen the interaction between the composites and HNPs. Furthermore, the random binding that occurred

Open Access Article. Published on 23 January 2026. Downloaded on 2/25/2026 12:13:14 PM.
This article is licensed under a Creative Commons Attribution-NonCommercial 3.0 Unported Licence.

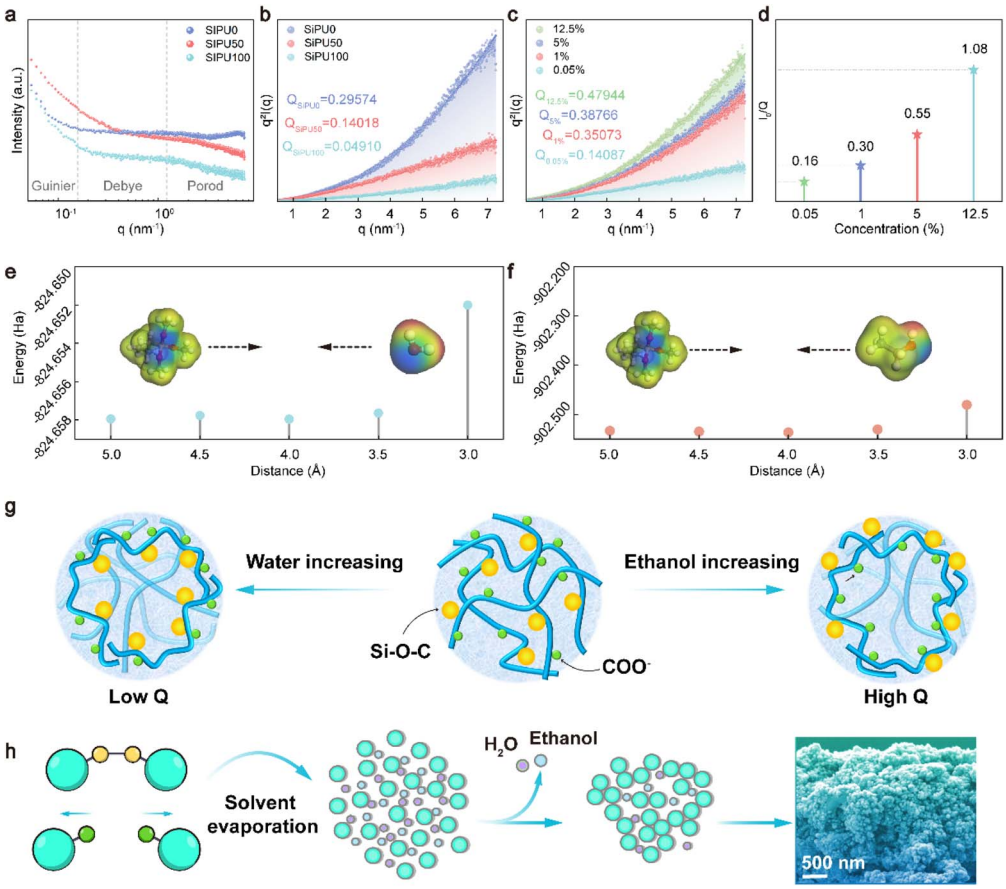

Fig. 4 Mechanism of SWDS formation from SiPU under the synergistic solvation of water and ethanol. (a) $I(q)$-q relationship of SiPU at different water and ethanol ratios. SiPU100 corresponds to a water-to-ethanol ratio of 100 : 1; SiPU50 corresponds to a ratio of 1 : 1; and SiPU0 corresponds to a ratio of 1 : 100. (b) $q^2I(q)$-q relationship of SiPU at different water to ethanol ratios. (c) $q^2I(q)$-q relationship of SiPU50 at different concentrations. (d) Relationship between I_0/Q and concentration of SiPU50. (e) Interaction energy between hydrophobic side groups and water molecules as a function of distance. (f) Interaction energy between hydrophobic side groups and ethanol molecules as a function of distance. (g) Schematic diagram of conformational changes of SiPU under the synergistic effect of water and ethanol solvents in a dilute particle system. (h) Schematic diagram of the transition process from a dilute particle model to a bicontinuous model, illustrating the formation of a broad distribution and stable surface roughness structure of SiPU.

during the solvent evaporation process was believed to contribute to the formation of a micro-meso scale rough structure, so we employed small-angle X-ray scattering (SAXS) to investigate this phenomenon. The principle of SAXS involves the scattering of incident X-rays within the material, where the scattering intensity varies with different scattering vectors. By analyzing these relationships, we were able to infer the relative fluctuations of electrons within the materials.

In dilute particle systems, we conducted SAXS experiments on SiPU (SP-5) and analyzed the impact of the water–ethanol ratio on molecular chain conformation. According to the theory of random coil conformations in polymer physics, the anionic waterborne polyurethane emulsions we prepared could be considered to exhibit a sea-island structure under the condition of dilute particles. Here, we assume that SiPU clusters are islands and the solvent is the sea. The islands, due to the anionic side groups, exhibit negative charge. Under constant concentration, altering the ratio of mixed solvents caused changes in the $I(q)$-q curve shape (Fig. 4a). When transformed into an integral form, it became evident that Q increased with the ethanol content (Fig. 4b). This indicates that the molecule adjusts its conformation to adapt to solvent variations, keeping the energy of the system at a lower state. We propose that the hydrophobic interaction of Si–O–C side groups is the primary driving force behind this behavior. By employing density functional theory to calculate the interaction energy between the alkoxy groups and two solvents, we find that the interaction energy between the alkoxy groups and water is significantly greater than that with ethanol (Fig. 4e–f and Table S2). Driven by this hydrophobic interaction, the hydrophobic side groups tended to invert toward the interior of the islands to maintain a low-energy conformation, while the corresponding negatively charged anionic side groups were located at the edge of the islands, where they were partially shielded by the solvation portion, resulting in a low Q value. As the ethanol content increased, these side groups that had been flipped inside the island reoriented back to the edge of the island, causing the

 This journal is © The Royal Society of Chemistry 2026

Open Access Article. Published on 23 January 2026. Downloaded on 2/25/2026 12:13:14 PM.
This article is licensed under a Creative Commons Attribution-NonCommercial 3.0 Unported Licence.

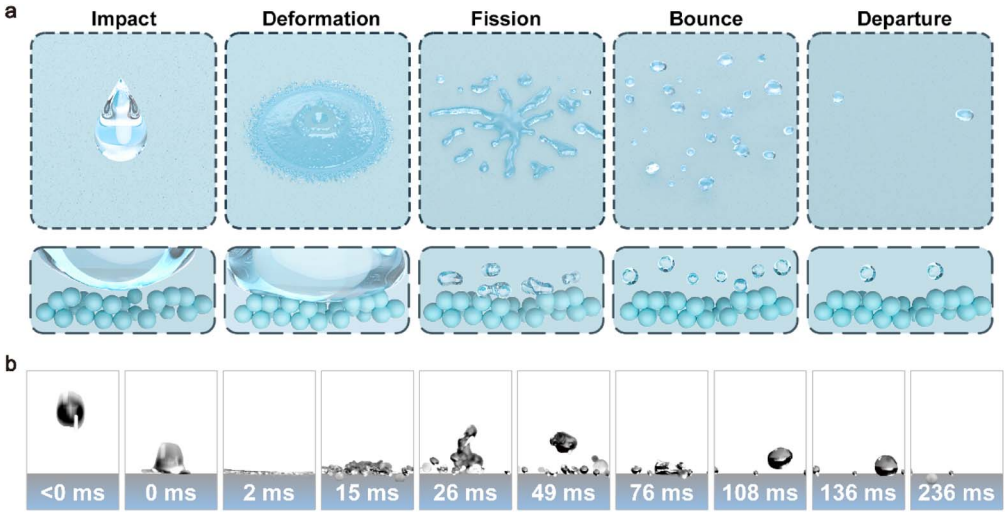

Fig. 5 Non-equilibrium wetting behavior of high-velocity ($v \approx 2.56$ m s^{-1}) water droplets on the surface of SP-5@HNP. (a) Schematic illustration of the non-equilibrium wetting processes of high-velocity water droplets on the surface of SP-5@HNP. (b) High-speed camera images depicting the non-equilibrium wetting of high-velocity water droplets on the surface of SP-5@HNP.

negatively charged anionic side groups to revert to the interior of the island, resulting in a higher Q value (Fig. 4g).

During the curing process of the coating, as the solvent evaporated, the concentration gradually increased, and the original sea-island structure progressively transformed into a bicontinuous model. Throughout this process, the Q value of the system increased with increasing concentration, indicating an overall increase in electron fluctuations within the system (Fig. 4c). This suggested that more COO^- groups were inverted inside the islands, and correspondingly, more Si–O–C bonds were flipped to the sea-island boundaries. These silicon oxygen bonds tended to crosslink, forming Si–O–Si bonds, which not only provided low surface energy but also ensured good mechanical stability. Moreover, the volume of the islands increased as the solvent evaporated (Fig. 4d). This phenomenon could be understood as several small islands approaching each other during solvent evaporation, with Si–O–C bonds at the island edges crosslinking to form larger island structures (Fig. 4h). The above SAXS results demonstrated that SiPU could provide low surface energy while forming multi-scale and stable surface roughness structures.

Sustainable value and scaling prospects

To further advance the application of the SWDS, we evaluated its performance under non-equilibrium wetting by high-velocity water droplets. High-velocity moving liquids are more prone to wetting and forming a new solid–liquid interface under the influence of impact force. In contrast, the SWDS allows the entire non-equilibrium wetting process to proceed in the order of impact, deformation, fission, rebound, and departure, which can prevent the aforementioned processes (Fig. 5a). High-speed camera images of SP-5@HNP under such conditions reveal that when the kinetic energy of a droplet exceeds its maximum diffusion state surface energy, the droplet will undergo volumetric fragmentation, thereby increasing its surface energy to consume the excess kinetic energy input. The resulting smaller droplets still retain a certain amount of kinetic energy, enabling their spontaneous detachment from the surface. This indicates that the SWDS can maintain its hydrophobicity even under high velocity impact, demonstrating its potential in the resistance to calendar aging (Fig. 5b). We further assessed the mechanical durability of the coating through two abrasion protocols: 50 cycles of finger rubbing and sandpaper abrasion under load.[45,46] In both tests, the coating showed no visible surface degradation (Fig. S16). Post-abrasion SEM imaging confirmed the preservation of its engineered rough microstructure (Fig. S17). High-velocity impact tests conducted on abraded samples revealed that the coating still exhibited excellent water repellency, remaining in a "non-wetting" state (Movie S7).

Further, we prepared a series of SWDS samples and exposed them to outdoor environments in ten cities across China, representing a range of distinct climatic conditions, to assess their long-term hydrophobicity. Given the limitations of contact angle measurements in describing hydrophobicity,[47] we employed the water adhesion ratio following non-equilibrium wetting as a more reliable indicator. The results demonstrated that under various climatic conditions, all samples maintained effective hydrophobicity for over 9 months, with water adhesion ratios not exceeding 1.2%. Notably, in Suzhou, a region characterized by high precipitation, the material exhibited an exceptionally low water adhesion ratio of 0.2% after 18 months of outdoor exposure (Movie S8). This indicates its outstanding resistance to calendar aging and highlights its potential for large-scale applications. Moreover, we observed a correlation between the water adhesion ratio and local climatic conditions. In areas with heavy rainfall, SWDS maintained a low water adhesion ratio even after prolonged outdoor exposure, while in regions with less precipitation, the material exhibited higher water adhesion and a faster rate of hydrophobicity degradation (Table S3). This inverse relationship between rainfall and water

Open Access Article. Published on 23 January 2026. Downloaded on 2/25/2026 12:13:14 PM.
This article is licensed under a Creative Commons Attribution-NonCommercial 3.0 Unported Licence.

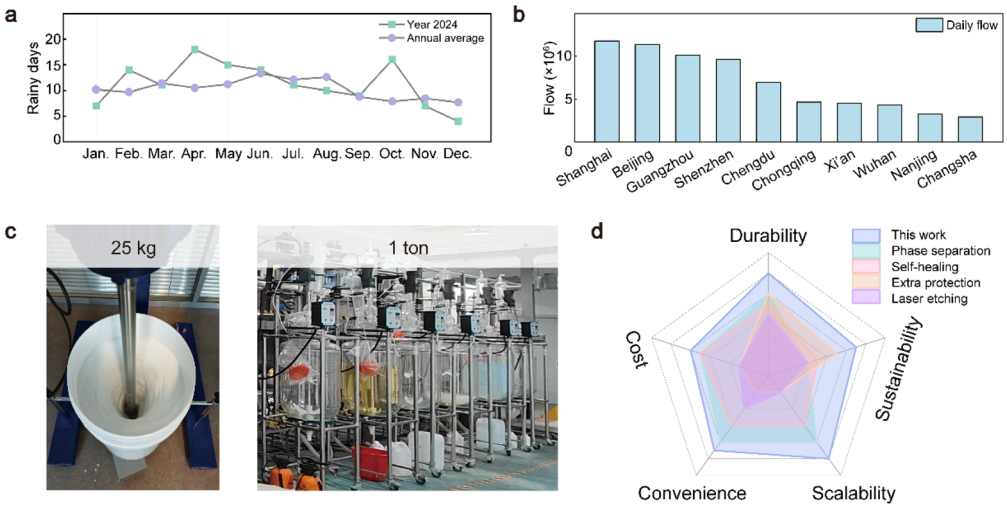

Fig. 6 Resistance to calendar aging and scalability of SWDS. (a) Annual precipitation days statistics of Wuxi city. (b) Passenger flow statistics of the top ten cities by single-day metro ridership. (c) Industrialized mass production of 25 kg and 1 ton of SWDS. (d) Comprehensive comparison of this work with other hydrophobic surface fabrication methods.

adhesion further supports the proposed mechanism of hydrophobic degradation due to non-equilibrium wetting. In regions with abundant rainfall, frequent rainfall events prevent the accumulation of contaminants on the surface, thereby extending their lifespan.

Given the performance and application potential of SWDS, we focus on scenarios where rainwater adhesion on umbrellas is a persistent issue, realizing the value of SWDS. Rainwater adhered to umbrellas has long been a nuisance when transferring from outdoors to indoors. This issue is particularly prominent in high-footfall areas such as subways and shopping malls, where a large number of umbrellas carrying residual rainwater enter indoor spaces. The accumulation of this water increases the burden of indoor humidity management and leads to additional carbon emissions. Moreover, indoor water accumulation can cause slippery floors, increase the risk of falls, and pose a threat to human health. High-power dryers are commonly employed to remove the residual water adhering to the floor surface in order to maintain dry conditions (Fig. S18). The only obvious solution to addressing these challenges seems to increase carbon emissions. We selected Wuxi, a city in East China, to assess how it tackles this challenge. According to government data (source: http://js.cma.gov.cn/dsjwz/wxs/qxfw_4632/wnfw/), the average annual rainy days in this region are about 10 days per month, and about one-third of the year is rainy. In 2024, two months experienced more than 15 days of rainfall (Fig. 6a). Taking Wuxi Metro, a typical indoor scenario, as an example, we examined the measures implemented by the metro system. According to tender information in 2023, Wuxi Metro procured 300 umbrella-bagging machines and wrapped wet umbrellas in plastic bags at the entrance to reduce their impact on indoor humidity (source: https://scm.wxmetro.net:3000/Purchase/BiddingA). However, this increases the consumption of plastic bags and creates an environmental burden. With the increase of metro traffic volume, this additional consumption also increases. We analyzed the top ten cities in terms of daily subway passenger flow in China, with Shanghai and Beijing each having over 10 million passengers daily (Fig. 6b). The resulting increase in carbon emissions from indoor humidity management in such high-volume metro systems is substantial and difficult to estimate. We applied a hydrophobic coating to the surface of the umbrella, creating a hydrophobic umbrella that can maintain almost no water on the surface even under high-velocity water impact (Fig. S19). This approach helps prevent additional carbon emissions associated with managing wet umbrellas, demonstrating significant potential for sustainability. Furthermore, we undertook large-scale production trials of SWDS. Through continuous process optimization, we successfully synthesized 25 kg of SWDS in the laboratory. Subsequently, utilizing larger equipment, we achieved a production of 1 ton of SWDS in a single day. This accomplishment establishes a foundation for its scalable application (Fig. 6c). Finally, we benchmarked our hydrophobic coating strategy against conventional approaches across five key dimensions: durability, cost, sustainability, convenience, and scalability[48,49] (Fig. 6d). Our strategy for constructing hydrophobic surfaces integrates multiple advantages and holds strong potential as a new material platform to advance sustainable development.

Conclusions

In summary, we propose a strategy that utilizes both equilibrium wetting and non-equilibrium wetting to describe hydrophobicity, which effectively addresses the issue of contact angle hysteresis caused by variations in liquid volume. By analyzing the energy pathways in non-equilibrium wetting, we identify that avoiding surface irreversibility induced by interfacial energy plays a crucial role in maintaining the long-term stability of hydrophobic surfaces. Key structural characteristics, such as

 This journal is © The Royal Society of Chemistry 2026

Open Access Article. Published on 23 January 2026. Downloaded on 2/25/2026 12:13:14 PM.
This article is licensed under a Creative Commons Attribution-NonCommercial 3.0 Unported Licence.

robust surface structures and micro-meso scale rough structures can prevent the formation of new interfaces during non-equilibrium wetting.

Building on this strategy, we developed a water-based SWDS resistant to calendar aging that maintained its hydrophobicity for up to 18 months. Furthermore, the application of SWDS to umbrella surfaces significantly reduced water adhesion, addressing the root causes of excessive carbon emissions and microplastic pollution associated with wet umbrella treatment. This approach provides valuable insights into the design of durable hydrophobic surfaces and holds significant potential for scalable manufacturing.

Materials and methods

Materials

Polytetrahydrofuran (PTMG, Mn ≈ 2000), isophorone diisocyanate (IPDI), and triethylamine (TEA) were purchased from Macklin. 2,2-Dihydroxymethylpropionic acid (DMPA), 3-aminopropyltriethoxysilane, *N*-(2-aminoethyl)-3-aminopropyltrimethoxysilane, tetraethyl orthosilicate, heptadecafluorodecyltrimethoxysilane (FAS-17), and ethanol were purchased from Aladdin.

Preparation of hydrophobic nanoparticles

Tetraethyl orthosilicate (TEOS) (0.5 g) and ammonia (0.02 g) were added to a 50 ml round-bottomed flask with 20 ml of a mixed solution of water and ethanol (1 : 100 v/v). The solution was heated in an oil bath at 40 °C for 24 hours to promote hydrolysis. Afterward, the solution was allowed to cool to room temperature. Finally, the mixture was filtered to obtain the preliminarily hydrolyzed silica nanoparticles. Heptadecafluorodecyltrimethoxysilane (FAS-17) (0.02 g), silica nanoparticles (0.2 g) and ammonia (0.01 g) were added to a round-bottom flask, followed by 100 mL of ethanol. The mixture was stirred at room temperature for 24 hours. Finally, the mixture was filtered and dried to obtain the hydrophobic nanoparticles (HNPs).

Preparation of SP emulsion

Polytetrahydrofuran (PTMG-2k) was heated under vacuum at 80 °C for 2 hours to remove trace amounts of water. Subsequently, isophorone diisocyanate (IPDI) was added to the mixture. The mixture was then thoroughly blended at 63 °C, followed by the addition of 3 drops of dibutyltin dilaurate (DBDT), and maintained at this temperature for 3 hours. Then, 2,2-dihydroxymethylpropionic acid (DMPA) was added, and the reaction was allowed to proceed for 2 hours. Subsequently, triethylamine (TEA) was added, and the reaction was allowed to proceed for 30 minutes. Triethylamine and *N*-(2-aminoethyl)-3-aminopropyl trimethoxysilane were added, and the reaction was continued for an additional hour. Finally, 3-aminopropyltriethoxysilane was added, and the mixture was stirred thoroughly. The resulting solution was then dropwise added to water to obtain the SP emulsion.

Preparation of SP@HNP

Hydrophobic nanoparticles (10 g) and ethanol (90 g) were added to a beaker and subjected to high-speed shear at 2000 rpm for 1 hour to obtain a homogeneous HNP ethanol dispersion. Subsequently, an SP emulsion with a solid content of 10% was added to the dispersion, and shearing was continued for an additional hour to obtain SP@HNP.

High-speed imaging of non-equilibrium wetting

High-speed camera images were obtained using a Phantom V711 high-speed camera. The light source selected was a Sidande 200W LED lamp, with the color temperature set at 4500 K.

Assessment of electronic fluctuations *via* small-angle X-ray scattering (SAXS)

Small-angle X-ray scattering (SAXS) experiments were performed with a high-flux small-angle X-ray scattering instrument (SAXSess mc2, Anton Paar). The total amplitude in the scattering equation can be described by the following formula:

$$A(q) = \sum_{i=1}^{N} e^{-\mathrm{iqr}} = \int \rho(r) e^{-\mathrm{iqr}} d^3 r \tag{1}$$

where $\rho(r)$ represents electron density at a distance r, q represents the magnitude of the scattering vector. Furthermore, the scattering intensity equation can be described by the following formula:

$$I(q) = \mathrm{AA}^* = V \int_0^\infty 4\pi \mathrm{r}^2 dr \cdot \gamma(r) \frac{\sin qr}{qr} \tag{2}$$

where $\gamma(r)$ represents the correlation function of electron fluctuations. This equation establishes a connection between the measurable external quantity of scattering intensity and the unobservable internal quantity of electron fluctuations. After performing the inverse Fourier transform and setting $r = 0$, we obtain the following formula:

$$V\gamma(0) = \frac{1}{2\pi^2} \int_0^\infty q^2 I(q) dq = V\langle \eta^2 \rangle \tag{3}$$

where $\langle \eta^2 \rangle$ represents the square of the total electron fluctuations. Once the structure of the material is determined, the total electron fluctuations within the material are also determined, along with the corresponding integral expression. This is defined as Q (invariant) and is used to describe the total electron fluctuations within the material.

Morphological and structural characterization

The surface morphology of the hydrophobic coating was characterized using scanning electron microscopy (SEM, ZEISS Sigma 300). The chemical structure of SP was characterized using Fourier transform infrared spectroscopy (FTIR, Bruker Tensor II). The periodic structure of SP was characterized using powder X-ray diffraction (PXRD, Bruker D8 ADVANCE). The

Open Access Article. Published on 23 January 2026. Downloaded on 2/25/2026 12:13:14 PM.
This article is licensed under a Creative Commons Attribution-NonCommercial 3.0 Unported Licence.

particle size distribution of the SP emulsion was characterized using dynamic light scattering (DLS, Brookhaven Instruments Corporation Instrument).

Computational methods

Geometry optimization and interaction energy calculations were performed using the DMol3 module in the Materials Studio software package, with a numerical basis set and the functional set to LDA-PWC. The convergence criterion for geometry optimization was set to 1×10^{-5} Ha.

Preparation of a hydrophobic umbrella

Hydrophobic coatings were applied to the surface of an unfolded umbrella using a pneumatic spray gun. The spray gun, with a nozzle diameter of 1 mm, was calibrated to achieve optimal airflow and atomization, ensuring the coating thickness was approximately 10 μm. The umbrella was then allowed to cure naturally at room temperature for 1 hour to form a hydrophobic umbrella.

Calculation of the water adhesion ratio

The hydrophobicity of the SWDS coating was assessed by calculating the water adhesion ratio, which represented the proportion of water that remained on the surface and cannot spontaneously detach during a non-equilibrium wetting process. A 50 cm × 50 cm glass plate was selected as the substrate, and its initial weight was measured and recorded as m_1 (g). The SWDS coating was applied to the surface of the glass plate, and after natural curing, the weight of the coated substrate was measured and recorded as m_2 (g). Next, 500 g of water was poured from a height of 1 meter directly above the coated surface, which was placed horizontally. The total weight of the system, including the water that remained adhered to the surface, was recorded as m_3 (g). The water adhesion ratio was calculated using the following equation:

$$\text{Water Adhesion Ratio} = \frac{m_3 - m_2}{m_2 - m_1} \tag{4}$$

Author contributions

Conceptualization: J. Y. Theoretical calculation and simulation: J. Y. and W. W. Fabrication and measurement: J. Y. and W. W. Data analysis: J. Y., W. W., Y. L., and Z. Y. Writing: J. Y. and W. W. Supervision: Q. Z. and X. J.

Conflicts of interest

There are no conflicts to declare.

Data availability

The authors confirm that the data supporting the findings of this study are available within the article and its supplementary information (SI): experimental details, characterization data and performance tests. Supplementary information is available. See DOI: https://doi.org/10.1039/d5ta09855f.

Acknowledgements

We thank the National Natural Science Foundation of China (Grant 52473112). The work was supported by the Fundamental Research Funds for the Central Universities.

References

1 H. Ye, E. J. Fetzer, S. Wong and B. H. Lambrigtsen, *Sci. Adv.*, 2017, **3**, e1600944.
2 Z. Yan, B. Wu, T. Li, M. Collins, R. Clark, T. Zhou, J. Murphy and G. Tan, *Sci. Adv.*, 2020, **6**, eaax4177.
3 S. Moon, N. Utsumi, J. H. Jeong, J. H. Yoon, S. S. Wang, H. Shiogama and H. Kim, *Sci. Adv.*, 2023, **9**, eadh4195.
4 E. Bevacqua, D. Maraun, M. I. Vousdoukas, E. Voukouvalas, M. Vrac, L. Mentaschi and M. Widmann, *Sci. Adv.*, 2019, **5**, eaaw5531.
5 N. Utsumi and H. Kim, *Nat. Clim. Change*, 2022, **12**, 436–440.
6 X. Lian, W. Zhao and P. Gentine, *Nat. Commun.*, 2022, **13**, 7642.
7 M. F. Ruiz-López, M. T. C. Martins-Costa, J. M. Anglada and J. S. Francisco, *J. Am. Chem. Soc.*, 2019, **141**, 16564–16568.
8 Y. Li, J. Liu, C. George, H. Herrmann, M. Gu, M. Yang, Y. Wang, A. Mellouki, Y. Pan, J. D. Felix, H. Kawashima, Z. Zhang, S. Wang and Y. Zeng, *Environ. Sci. Technol.*, 2023, **57**, 16424–16434.
9 M. Zhou, L. Zhang, L. Zhong, M. Chen, L. Zhu, T. Zhang, X. Han, Y. Hou and Y. Zheng, *Adv. Mater.*, 2024, **36**, e2305322.
10 B. Li, L. Hua, Y. Tu and R. Wang, *Joule*, 2019, **3**, 1427–1436.
11 M. Posani, V. Voney, P. Odaglia, Y. Du, A. Komkova, C. Brumaud, B. Dillenburger and G. Habert, *Nat. Commun.*, 2025, **16**, 425.
12 T. Young, *Philos. Trans. R. Soc. London*, 1805, **95**, 65–87.
13 R. Wenzel, *Ind. Eng. Chem.*, 1936, **28**, 988–994.
14 A. Cassie and S. Baxter, *Trans. Fara Soc.*, 1944, **40**, 0546–0550.
15 T. Mouterde, P. Lecointre, G. Lehoucq, A. Checco, C. Clanet and D. Quéré, *Nat. Commun.*, 2019, **10**, 1410.
16 J. Luo, S.-Y. Wu, L. Xiao and Z.-L. Chen, *Int. J. Mech. Sci.*, 2021, **197**, 106333.
17 C. Ye, V. S. D. Voet, R. Folkersma and K. Loos, *Adv. Mater.*, 2021, **33**, e2008460.
18 C. Peng, Z. Chen and M. K. Tiwari, *Nat. Mater.*, 2018, **17**, 355–360.
19 W. Chen, P. Zhang, R. Zang, J. Fan, S. Wang, B. Wang and J. Meng, *Adv. Mater.*, 2020, **32**, e1907413.
20 D. Wang, Q. Sun, M. J. Hokkanen, C. Zhang, F. Y. Lin, Q. Liu, S. P. Zhu, T. Zhou, Q. Chang, B. He, Q. Zhou, L. Chen, Z. Wang, R. H. A. Ras and X. Deng, *Nature*, 2020, **582**, 55–59.
21 X.-J. Guo, C.-H. Xue, S. Sathasivam, K. Page, G. He, J. Guo, P. Promdet, F. L. Heale, C. J. Carmalt and I. P. Parkin, *J. Mater. Chem. A*, 2019, **7**, 17604–17612.
22 X. Zhang, Y. Lei, C. Li, G. Sun and B. You, *Adv. Funct. Mater.*, 2021, **32**, 2110830.
23 Q. Zhang, X. Bai, Y. Li, X. Zhang, D. Tian and L. Jiang, *ACS Nano*, 2022, **16**, 16843–16852.

 This journal is © The Royal Society of Chemistry 2026

Open Access Article. Published on 23 January 2026. Downloaded on 2/25/2026 12:13:14 PM.
This article is licensed under a Creative Commons Attribution-NonCommercial 3.0 Unported Licence.

24 W. Zhang, J. Gao, Y. Deng, L. Peng, P. Yi, X. Lai and Z. Lin, *Adv. Funct. Mater.*, 2021, **31**, 1–8.
25 Y. Guan, B. Bi, D. Qiao, S. Cao, W. Zhang, Z. Wang, H. Zeng and Y. Li, *J. Mater. Chem. A*, 2024, **12**, 9850–9862.
26 H. Li, L. Xin, J. Gao, Y. Shao, Z. Zhang and L. Ren, *Small*, 2024, **20**, e2309012.
27 W. Li, K. Liu, Y. Zhang, S. Guo, Z. Li and S. C. Tan, *Chem. Eng. J.*, 2022, **446**, 137195.
28 L. Qin, N. Chen, X. Zhou and Q. Pan, *J. Mater. Chem. A*, 2018, **6**, 4424–4431.
29 J. Wei, J. Zhang, X. Cao, J. Huo, X. Huang and J. Zhang, *Nat. Commun.*, 2023, **14**, 2862.
30 Y. Wang, R. Sun, W. Zhao, X. Lu, W. Xiao, F. Meng, X. Zhan, J. Lu, F. Gao and Q. Zhang, *Adv. Funct. Mater.*, 2025, **35**, 2418795.
31 J. Liu, Z. Tong, F. Gao, J. Wang, J. Hu, L. Song, Y. Hou, J. Lu, X. Zhan and Q. Zhang, *Adv. Mater.*, 2024, **36**, 2401982.
32 L. Qiao, M. Wang, Z. Zhou and Z. He, *J. Hazard. Mater.*, 2025, **495**, 138909.
33 A. Lafuma and D. Quéré, *Nat. Mater.*, 2003, **2**, 457–460.
34 J. Rahlff, S. P. Esser, J. Plewka, M. E. Heinrichs, A. Soares, C. Scarchilli, P. Grigioni, H. Wex, H.-A. Giebel and A. J. Probst, *Nat. Commun.*, 2023, **14**, 6354.
35 D. Öner and T. J. McCarthy, *Langmuir*, 2000, **16**, 7777–7782.
36 F. Xia, L. Feng, S. Wang, T. Sun, W. Song, W. Jiang and L. Jiang, *Adv. Mater.*, 2006, **18**, 432–436.
37 Y. Zhu, J. Zhang, Y. Zheng, Z. Huang, L. Feng and L. Jiang, *Adv. Funct. Mater.*, 2006, **16**, 568–574.
38 X. Q. Feng, X. Gao, Z. Wu, L. Jiang and Q. S. Zheng, *Langmuir*, 2007, **23**, 4892–4896.
39 X. Hong, X. Gao and L. Jiang, *J. Am. Chem. Soc.*, 2007, **129**, 1478–1479.
40 S. Wang and L. Jiang, *Adv. Mater.*, 2007, **19**, 3423–3424.
41 Q. Zhang, E. G. Xu, J. Li, Q. Chen, L. Ma, E. Y. Zeng and H. Shi, *Environ. Sci. Technol.*, 2020, **54**, 3740–3751.
42 Y. Wang, H. Okochi, Y. Tani, H. Hayami, Y. Minami, N. Katsumi, M. Takeuchi, A. Sorimachi, Y. Fujii, M. Kajino, K. Adachi, Y. Ishihara, Y. Iwamoto and Y. Niida, *Environ. Chem. Lett.*, 2023, **21**, 3055–3062.
43 L. E. Revell, P. Kuma, E. C. Le Ru, W. R. C. Somerville and S. Gaw, *Nature*, 2021, **598**, 462–467.
44 Z. Chen, M. Elektorowicz, C. An and X. Tian, *Environ. Sci. Technol.*, 2023, **57**, 3176–3186.
45 P. Wang, M. Chen, H. Han, X. Fan, Q. Liu and J. Wang, *J. Mater. Chem. A*, 2016, **4**, 7869–7874.
46 J. Ju, X. Yao, X. Hou, Q. Liu, Y. S. Zhang and A. Khademhosseini, *J. Mater. Chem. A*, 2017, **5**, 16273–16280.
47 I. U. Vakarelski, N. A. Patankar, J. O. Marston, D. Y. C. Chan and S. T. Thoroddsen, *Nature*, 2012, **489**, 274–277.
48 F. Chen, Y. Wang, Y. Tian, D. Zhang, J. Song, C. R. Crick, C. J. Carmalt, I. P. Parkin and Y. Lu, *Chem. Soc. Rev.*, 2022, **51**, 8476–8583.
49 W. Zhang, D. Wang, Z. Sun, J. Song and X. Deng, *Chem. Soc. Rev.*, 2021, **50**, 4031–4061.